JOURNAL OF QUATERNARY SCIENCE (2026) 1–15 ISSN 0267-8179. DOI: 10.1002/jqs.70070

JQS Journal of Quaternary Science QRA Quaternary Research Association

Reconstructing the Holocene explosive eruptive history of the Erciyes volcano (Turkey) using proximal and distal tephra records

IVAN SUNYÉ-PUCHOL,[1]* RENGIN ÖZSOY-ÜNAL,[1] XAVIER BOLÓS,[2] VICTORIA C. SMITH,[3] EFE AKKAS,[4] LORENZO TAVAZZANI,[5] JAN AYMERICH,[2,6] MANUELA NAZZARI,[7] PIERRE LACAN,[8,9] VICTORIA CULLEN,[10] OLIVIER BACHMANN,[5] PIERGIORGIO SCARLATO[7] and SILVIO MOLLO[1,7]

[1]Department of Earth Sciences, Sapienza University of Rome, Rome, Italy
[2]Geosciences Barcelona (GEO3BCN), CSIC, Barcelona, Catalonia, Spain
[3]School of Archaeology, University of Oxford, 1 South Parks Road, Oxford, OX1 3TG, United Kingdom
[4]Department of Geological Engineering, Hacettepe University, Ankara, Turkey
[5]Institute of Geochemistry and Petrology, ETH Zürich, Zurich, Switzerland
[6]Department of Mineralogy, Petrology and Applied Geology, University of Barcelona, Barcelona, Spain
[7]Istituto Nazionale di Geofisica e Vulcanologia (INGV), Sezione di Roma1, Rome, Italy
[8]Instituto de Geociencias (IGEO), Universidad Nacional Autónoma de México (UNAM), Querétaro, México
[9]Geosciences Montpellier, University of Montpellier–CNRS, Montpellier, France
[10]Department of Biochemistry, University of Oxford, Oxford, UK

Received 16 October 2025; Revised 17 March 2026; Accepted 20 March 2026

ABSTRACT: Mount Erciyes, the largest active volcano of Central Anatolia (Turkey), erupted explosively during the Holocene, producing the Karagüllü, Perikartin and Dikkartin tuff rings. Even though major cities like Kayseri and its ~1 million residents sit directly on these pyroclastic deposits, the timing and magnitude of the explosive eruptions have remained poorly constrained. To assess regional ash dispersal and improve the Erciyes Holocene explosive eruptive history, here, we integrate tephrostratigraphic observations, glass shard geochemistry and radiocarbon dating of organic-rich palaeosols. Our results indicate that the Karagüllü tuff ring formed around 11 258 ± 56 cal yr BP, followed by the Perikartin eruption at 9700 ± 100 cal yr BP. Although no stratigraphic contacts are evident with the other eruption deposits and there is no radiocarbon datable material in or below Dikkartin, its glass composition matches the regional S1 tephra dated to approximately 9000 cal yr BP, and this date can be assigned to the Dikkartin eruption. Distal correlations also confirm the widespread dispersal of the Karagüllü tephra, as it is identified as a cryptotephra layer in the Black Sea and Romanian lakes, indicating that the Central Anatolian eruptions dispersed volcanic ash over several hundred to more than a 1000 km across Europe and the eastern Mediterranean in the early Holocene. These correlations enhance the regional tephrochronological framework and underscore the need to re-assess volcanic hazards in Central Turkey and surrounding areas.

KEYWORDS: Black Sea tephra record; Central Anatolian Volcanic Province (CAVP); tephrochronological correlations; volcanic glass geochemistry; volcanic hazard assessment

INTRODUCTION

To comprehend the likely future eruptive activity at volcanoes and the associated hazards, it is crucial to understand the tempo, style and magnitude of previous activity. Detailed reconstructions of eruptive histories have been successfully achieved at several well-studied volcanic systems, particularly through the integration of proximal tephrostratigraphy and distal tephrochronological correlations. A benchmark example is the Campanian Volcanic Province (Italy), where combined stratigraphic, geochemical and chronological approaches have enabled robust reconstructions of explosive activity at Campi Flegrei, Somma-Vesuvius and Ischia volcanoes (e.g., Orsi et al., 2004; 2022; Smith et al., 2011; Scarpati et al., 2013, 2020), supported by widespread distal tephra correlations across the Mediterranean region (Satow et al., 2015; Albert et al., 2015; Monaco et al., 2021). Similarly, comprehensive eruptive reconstructions have been carried out at several other active and high-risk volcanic systems, including Santorini (Greece; Druitt et al., 1999; Wulf et al., 2020), Ilopango (El Salvador; e.g., Suñé-Puchol et al., 2019a, 2019b; Pedrazzi et al., 2019; Smith et al., 2020) and Popocatépetl (Mexico; Sunyé-Puchol et al., 2022), among others.

Despite these advances, detailed information remains lacking for many hazardous volcanoes worldwide, hindering robust reconstructions of their eruptive histories. One such case is Mount Erciyes, the largest active volcano of the Central Anatolian Volcanic Province (CAVP) in Turkey (Innocenti et al., 1975; Pasquaré et al., 1988; Le Pennec et al., 1994; Fig. 1(a),(b)). Mount Erciyes has been considerably active over a long period of time. It is a large composite volcano that extends to 3917 m asl and has a basal diameter of ~45 km. Its central crater, together with associated cones, domes, lava flows and pyroclastic deposits, was emplaced during the Quaternary within the 14 × 18 km Koç Dağ caldera (Fig. 1(c)). This caldera collapsed 2.73 ± 0.04 Ma

*Correspondence: Ivan Sunyé-Puchol, as above.
Email: ivan.sunyepuchol@uniroma1.it

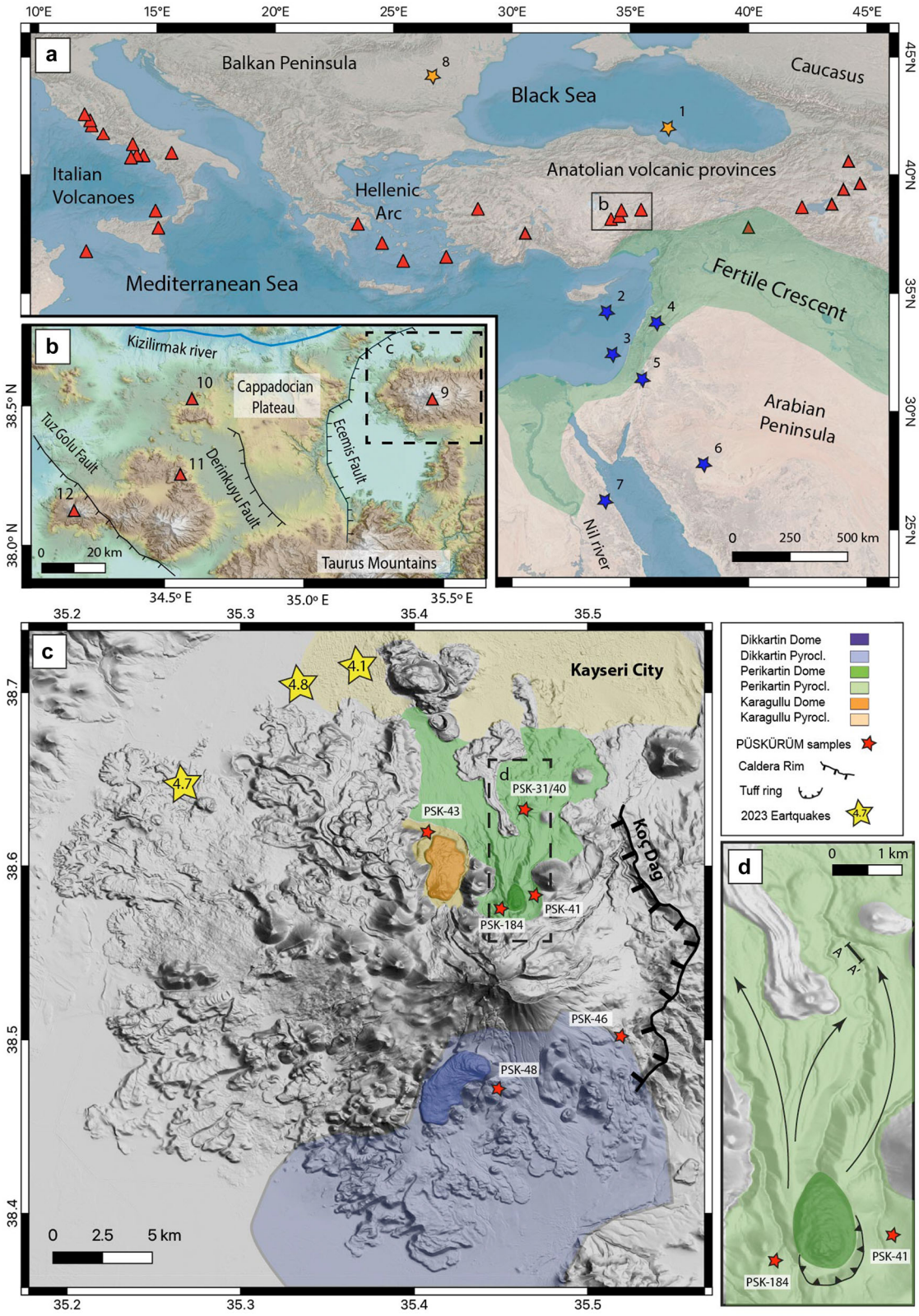

Figure 1. Study area. (a) Map of the Eastern Mediterranean showing the main Quaternary volcanoes (red triangles) and the sedimentary records in which Central Anatolian tephras have been found, including the S1 (blue stars) and BSC_079 (orange stars) from Erciyes volcano. 1 = Black Sea (M72/5-25-GC1, Cullen et al., 2014); Mediterranean Sea cores: 2 = M51/3-SL114 (Schmidt, 2007) and 3 = M51/3-SL112 (Hamann et al., 2010); 4 = Yammouneh basin, Lebanon (Develle et al., 2009); 5 = Dead Sea and 6 = Tayma palaeolake, Saudi Arabia (Neugebauer et al., 2017); 7 = Sodmein caves, Egypt (Barton et al., 2015); and 8 = Lakes Lia and Brazi, Romania (Kearney et al., 2024). (b) Central Anatolian Volcanic Province (CAVP), including Erciyes (9), Acigöl (10), Golludag (11) and Hasandag (12) volcanoes (numbering in panel B continues from panel A for clarity). (c) Map of Erciyes volcano showing the three Holocene eruption deposits (Karagüllü, Perikartin and Dikkartin), the city of Kayseri and the sampling location (red stars), including (d) the Hacilar site (A–A'). Maps A and C after Friedrichs et al., 2021. [Color figure can be viewed at wileyonlinelibrary.com]

ago (Sen et al., 2003; Friedrichs et al., 2020, 2021) following the emission of the 40 km^3 Valibaba Tepe ignimbrite (Sen et al., 2003). Prior to this caldera-forming eruption, the Koç Dağ volcano emplaced widespread basaltic, andesitic and dacitic lava flows (Sen et al., 2003).

The most recent large eruptions of Erciyes are represented by three rhyolitic tuff rings—Karagüllü, Perikartin and Dikkartin—formed from explosive activity during the Holocene (Sen et al., 2003; Sarikaya et al., 2019; Friedrichs et al., 2020). These structures, which were generated mainly by phreatomagmatic activity, were in some cases preceded by a Plinian phase, such as Dikkartin, with a 20–25 km eruption column (Ersoy et al., 2019; see Table 1 for more details about these Holocene tuff ring eruptions and their related deposits). Located on the northern and southern flanks of the volcano (Fig. 1(c)), the tuff rings were later partially obliterated by the emplacement of syn- to post-intra-crater lava domes, which generated block-and-ash flows down the slopes of Erciyes (Sarikaya et al., 2019). These lava domes are interpreted to represent the effusive phase of the same eruptive episode that produced the tuff rings, marking the transition from explosive to effusive activity (Sarikaya et al., 2019). The city of Kayseri, with nearly one million inhabitants, is built directly above pyroclastic deposits from the Karagüllü and Perikartin eruptions (Fig. 1(c)), highlighting the importance of reconstructing the recent eruptive history of Erciyes for volcanic hazard assessments in the Cappadocian region (Fig. 1(b)). This urgency is further underscored by proposed historical eruptions, which appear to be depicted on Roman coins minted during the reign of Emperor Tiberius (AD 14–37; Olmstead et al., 1907; Friedrichs et al., 2021), and by volcano-tectonic earthquakes reported in 2023 (Whitney et al., 2023; Petersen et al., 2023; Fig. 1(c)).

Although the three Holocene tuff rings have been dated using cosmogenic (Sarikaya et al., 2019) and radiogenic methods (U/Th–He in zircons; Friedrichs et al., 2020, 2021), these age estimates lack the precision needed to resolve the sequence of the recent substantial eruptions and their timing (Table 1). In this study, we conducted a detailed tephrostratigraphic and glass compositional investigation of the proximal Karagüllü, Perikartin and Dikkartin pyroclastic deposits, aiming to (i) establish their stratigraphic relationships and relative eruption ages by logging well-exposed outcrops such as the Hacilar site (Fig. 2); and (ii) obtain absolute ages from radiocarbon-dated, organic-rich palaeosols. However, due to limited exposures, no direct stratigraphic contacts among the three tuff ring deposits were observed, and suitable material for radiocarbon dating was not readily available. In such cases, geochemical fingerprinting of tephra enables correlations with well-dated distal sedimentary records, providing chronological constraints to refine the eruption timings (e.g., Lowe, 2011).

Over the past two decades, several tephrochronological studies in Anatolia and adjacent regions have linked distal tephras to the Holocene tuff-ring eruptions of Erciyes (Table 1). A prominent example is the widespread S1 tephra, which is macroscopically visible in the Eastern Mediterranean deep-sea sediment cores (Schmidt, 2007; Hamann et al., 2010) and occurs as cryptotephra in the Sodmein caves, Egypt (Barton et al., 2015), the Yammouneh basin, Lebanon (Develle et al., 2009), the Tayma palaeolake, Saudi Arabia, and the Dead Sea (Neugebauer et al., 2017). Based on major element glass geochemistry of proximal deposits, the S1 tephra has been attributed to Dikkartin eruption (e.g., Hamann et al., 2010; Neugebauer et al., 2017). Similarly, the BSC_079 tephra from the Black Sea has been correlated with either Karagüllü or Perikartin (Cullen et al., 2014). However, recent studies on proximal deposits (i.e., Friedrichs et al., 2020) pointed out that the glass chemistry of Perikartin is indistinguishable from that of Dikkartin, rather than from Karagüllü. This finding suggests that Perikartin may represent an alternative source of the S1 tephra instead of the source of the BSC_079 tephra. However, these proposed correlations remained tentative, as existing proximal tephrostratigraphic frameworks and geochemical data sets were incomplete and partly inconsistent, and are largely based on major element data. In contrast to previous work, here, we produce accurate and precise major and trace element glass data sets of the proximal Erciyes Holocene eruption deposits by collecting fresh pumice clasts from each tuff ring beneath the post-eruptive lava domes for glass geochemistry (sampling sites shown in Fig. 1(c)).

Here, we aim to re-assess previously proposed distal correlations for Erciyes tephras and evaluate whether additional correlations are supported by the data, with the goal of refining the chronology and magnitude estimates of its Holocene explosive eruptions. We also assess the potential

Table 1. Main parameters of the Erciyes Holocene tuff ring eruptions and related deposits.

Parameters	Karagüllü	Perikartın	Dikkartın
Location	Northern flank [1,2]	Northern flank [1,2]	Southern flank (1,2)
Age (ka)	5.5–11.4 (36Cl)[2]; 9.4 ± 1.3 U/Th–He [4,5]	9.7 ± 0.1 cal BP (14 C) [2]	7.0–10.8 (36Cl)[2]; 8.9 ± 0.5 (U/Th–He) [4,5]
Crater diameter	1.7 km [1,2]	1.2 km [1,2]	0.6 km [1,2]
Eruption style	Tuff ring + lava dome [1,2]	Tuff ring + lava dome [1,2]	Plinian + tuff ring + dome [3]
Initial phase	No Plinian, phreatomagmatic [1,2]	No Plinian, phreatomagmatic [1,2]	Plinian, 20–25 km column + phreatomagmatic [3]
Main deposits	Fallout, surges, lava dome and flows [1,2]	Fallout, lithic-rich PDCs dominated, lava dome and flows [1,2]	Plinian fallout, PDCs, lava dome and flows [3]
Deposit colours	White–pink pumice [1,2]	Pink/white pumice, lithic breccias [1,2]	White, pink, grey pumice, obsidian [1,2,3]
Thickness (proximal)	5–7 m of intercalated PDCs and fallouts [1,2]	>3–5 m of valley-fill breccias and PDCs [1,2]	~15 m fallout + >3 m PDCs [3]
Dispersal	Local to regional; cryptotephra in Black Sea debated [5,6]	Local to regional; S1 and Black Sea tephra correlation debated [5]	Widespread; correlated to S1 tephra >600–1300 km [5]
Dome extrusion	9.8 km^2, 5.2 km long, 0.7 km^3 [1,2]	6.6 km^2, 3.5 km long, 0.08 km^3 [1,2]	1.1 km^2, 1.3 km long, 0.8–1.0 km^3 [1,2,3]
Mineralogy/ Chemistry	Plag, Opx, Amph; 68%–72% SiO_2 [1,2,4,5]	Plag, Opx, Amph; ~70% SiO_2 [1,2,4,5]	Plag, Opx, Amph; ~70% SiO_2 [1,2,4,5]
Special notes	Distinct composition	Overlapping Dikkartin composition	S1 correlation [5]; VEI ~ 5 [3]

1 = Şen et al. 2003; 2 = Sarıkaya et al., 2019; 3 = Ersoy et al. 2019; 4 and 5 = Friedrichs et al. 2020, 2021; 6 = Cullen et al., 2014.

Table 2. Major and trace element compositions (average and 1σ standard deviation) of glass shards from proximal deposits, the Hacilar outcrop and Black Sea core samples.

Sample	PSK-32		PSK-33		PSK-34		PSK-35		PSK-36		PSK-37		PSK-38		PSK-39		PSK-41		PSK-43		PSK-48		PSK-184		BSC-079	
Outcrop	Hacilar		Hacilar		Hacilar		Hacilar		Hacilar		Hacilar		Hacilar		Hacilar		Tuff ring		Tuff ring		Tuff ring		Tuff ring		Black sea core	
Unit	Karagüllü		Karagüllü		Karagüllü		Karagüllü		Reworked		Perikartın		Perikartın		Perikartın		Perikartın		Karagüllü		Dikkartın		Perikartın		Karagüllü	
wt.%		±		±		±		±		±		±		±		±		±		±		±		±		±
SiO_2	77.04	0.64	77.04	0.40	76.66	0.49	76.56	0.34	76.85	0.50	75.20	0.50	75.41	0.70	75.38	1.11	75.33	0.51	77.25	0.23	75.01	0.22	74.85	0.74	77.44	0.40
TiO_2	0.13	0.07	0.13	0.06	0.16	0.05	0.14	0.06	0.12	0.04	0.21	0.06	0.20	0.02	0.19	0.02	0.13	0.10	0.15	0.05	0.24	0.05	0.22	0.05	0.13	0.03
Al_2O_3	13.15	0.39	12.85	0.29	12.99	0.30	13.14	0.23	12.79	0.32	13.75	0.32	13.74	0.48	13.84	0.79	13.98	0.27	12.84	0.16	13.79	0.19	13.92	0.61	12.76	0.26
FeO	0.92	0.07	0.96	0.09	0.94	0.07	0.95	0.07	0.96	0.09	1.29	0.10	1.32	0.10	1.19	0.16	1.13	0.10	0.91	0.07	1.33	0.07	1.35	0.11	0.95	0.08
MnO	0.03	0.03	0.04	0.03	0.03	0.02	0.04	0.02	0.04	0.03	0.03	0.03	0.03	0.02	0.04	0.02	0.03	0.02	0.03	0.03	0.04	0.03	0.04	0.02	0.04	0.03
MgO	0.22	0.03	0.22	0.03	0.23	0.03	0.23	0.04	0.22	0.04	0.33	0.05	0.34	0.05	0.30	0.09	0.35	0.05	0.21	0.05	0.36	0.03	0.37	0.05	0.23	0.04
CaO	0.96	0.13	1.04	0.10	1.09	0.11	1.11	0.07	1.03	0.13	1.38	0.13	1.38	0.23	1.40	0.36	1.31	0.14	1.01	0.09	1.44	0.07	1.47	0.11	1.04	0.09
Na_2O	3.66	0.17	3.72	0.10	3.93	0.16	3.85	0.10	3.98	0.17	4.05	0.11	3.86	0.15	4.00	0.29	4.12	0.14	3.72	0.11	4.13	0.10	3.99	0.18	3.54	0.14
K_2O	3.73	0.09	3.82	0.11	3.80	0.14	3.80	0.13	3.82	0.16	3.54	0.14	3.68	0.17	3.64	0.29	3.43	0.16	3.73	0.10	3.47	0.09	3.51	0.12	3.83	0.13
P_2O_5	0.04	0.02	0.03	0.02	0.04	0.03	0.04	0.02	0.04	0.02	0.07	0.03	0.06	0.05	0.07	0.04	0.05	0.02	0.03	0.02	0.03	0.02	0.14	0.17	0.08	0.06
ppm		±		±				±		±		±		±		±		±		±		±		±		±
Li	33.48	12.26	42.40	12.88	n.d.	n.d.	29.43	12.98	43.74	3.81	34.10	7.50	31.24	10.56	35.11	11.85	47.21	43.25	40.29	9.79	38.55	5.64	37.73	6.01	45.37	3.70
B	34.14	13.46	43.42	11.28	n.d.	n.d.	32.16	12.58	41.53	1.56	32.07	3.32	32.04	12.32	32.82	10.72	33.80	6.48	38.06	3.69	34.39	2.62	34.83	5.84	56.19	16.23
Sc	1.56	0.83	7.92	28.91	n.d.	n.d.	8.23	28.77	2.40	0.95	9.25	30.09	2.17	0.73	1.99	0.71	13.44	36.47	10.09	31.54	8.87	35.25	2.31	0.44	1.63	0.20
V	2.15	0.95	29.87	132.33	n.d.	n.d.	18.52	58.52	4.37	3.54	26.23	83.90	5.82	2.11	5.06	1.71	30.46	90.78	39.66	156.33	15.62	50.81	6.84	1.04	2.77	0.68
Cr	3.94	bdl	281.33	387.46	n.d.	n.d.	9.65	2.25	bdl	bdl	11.11	bdl	8.69	1.19	bdl	bdl	36.14	6.84	208.13	362.39	27.12	32.49	8.48	4.46	7.51	7.80
Co	0.68	0.36	5.15	19.81	n.d.	n.d.	4.67	15.49	1.36	1.45	5.91	20.38	1.45	0.52	1.24	0.40	8.90	25.25	12.11	31.73	3.96	14.08	1.50	0.39	1.27	0.20
Ni	1.62	1.44	61.69	115.29	n.d.	n.d.	12.74	18.81	bdl	bdl	46.43	50.65	2.35	bdl	bdl	bdl	51.86	67.86	70.98	93.68	76.37	bdl	2.42	bdl	7.28	6.29
Zn	25.13	20.34	37.37	51.38	n.d.	n.d.	40.71	70.25	30.62	4.67	40.20	58.51	25.21	10.33	27.24	9.78	68.47	89.86	58.09	126.90	42.72	65.79	32.93	9.10	24.33	8.95
Rb	121.38	46.99	160.39	57.91	n.d.	n.d.	120.23	47.48	156.82	4.28	123.61	32.45	123.32	46.82	130.18	47.25	131.49	44.09	132.13	40.60	133.17	26.93	140.46	20.10	148.18	5.20
Sr	88.30	8.67	96.58	15.67	n.d.	n.d.	89.82	23.40	97.46	9.74	147.59	103.82	111.82	8.52	117.47	12.99	125.99	28.72	86.83	27.70	123.33	30.11	121.69	10.39	98.96	19.51
Y	10.93	4.38	18.89	20.48	n.d.	n.d.	26.90	57.34	15.50	2.35	25.75	52.70	14.21	5.28	14.29	5.18	31.34	61.78	17.63	20.78	25.63	62.54	15.99	2.42	13.88	1.08
Zr	63.07	24.31	89.35	24.73	n.d.	n.d.	85.45	44.30	82.13	9.70	128.51	30.75	132.47	45.09	130.96	46.00	136.17	34.26	70.90	16.76	126.87	25.42	152.55	19.64	78.51	4.84
Nb	9.01	3.43	12.31	3.33	n.d.	n.d.	10.45	4.76	11.86	0.55	11.50	3.40	10.78	4.00	10.88	3.93	11.83	3.35	10.36	2.11	11.45	2.48	11.86	1.69	11.09	0.42
Cs	6.05	2.40	8.16	2.28	n.d.	n.d.	6.15	1.88	7.78	0.33	5.58	1.46	5.73	2.13	5.84	2.13	6.18	1.06	6.79	1.54	6.34	0.51	6.45	0.97	7.32	0.21
Ba	432.21	152.95	572.57	167.26	n.d.	n.d.	450.91	168.42	556.93	33.29	496.95	114.14	507.09	188.50	529.80	172.96	532.97	164.96	464.81	134.34	524.62	106.01	570.57	67.34	543.35	16.02
La	23.87	8.96	31.60	8.84	n.d.	n.d.	28.06	12.34	30.39	1.87	26.53	2.48	27.60	10.09	27.94	9.10	28.25	6.24	25.88	6.46	27.69	2.83	30.82	3.70	29.83	1.66
Ce	41.40	15.62	56.23	14.98	n.d.	n.d.	52.99	29.90	53.95	3.34	50.73	16.74	48.41	17.64	49.63	17.07	53.83	19.39	59.12	63.89	52.79	17.41	54.53	7.56	52.31	3.52
Pr	3.99	1.54	5.62	1.69	n.d.	n.d.	5.94	4.92	5.27	0.34	5.52	3.86	4.84	1.78	4.92	1.69	6.18	4.35	4.82	1.44	5.62	4.12	5.47	0.74	5.04	0.40
Nd	12.52	4.96	18.70	8.56	n.d.	n.d.	22.57	26.51	17.36	1.48	20.44	22.68	15.46	5.85	15.74	5.66	23.33	26.60	16.60	8.89	20.29	24.05	17.83	2.49	15.80	1.47
Sm	2.13	0.91	3.46	3.03	n.d.	n.d.	4.89	8.67	2.96	0.37	4.55	8.09	2.74	0.93	2.73	0.98	5.34	9.32	3.28	3.44	4.44	9.18	3.02	0.43	2.74	0.35
Eu	0.39	0.08	0.59	0.62	n.d.	n.d.	0.78	1.27	0.48	0.08	0.83	1.20	0.48	0.11	0.51	0.11	0.91	1.46	0.60	0.81	0.71	1.03	0.53	0.07	0.45	0.07
Gd	1.71	0.73	3.12	3.94	n.d.	n.d.	5.00	10.52	2.47	0.30	4.37	9.33	2.32	0.85	2.27	0.71	5.27	11.18	2.97	4.10	4.22	10.46	2.52	0.53	2.17	0.29
Tb	0.27	0.09	0.48	0.60	n.d.	n.d.	0.73	1.64	0.40	0.10	0.70	1.52	0.34	0.12	0.37	0.12	0.86	1.78	0.45	0.65	0.67	1.81	0.40	0.05	0.34	0.05
Dy	1.65	0.61	3.13	4.28	n.d.	n.d.	4.89	11.14	2.48	0.57	4.51	9.97	2.37	0.92	2.22	0.69	5.35	11.65	3.04	4.47	4.51	12.02	2.52	0.42	2.15	0.22
Ho	0.35	0.14	0.62	0.82	n.d.	n.d.	0.95	2.15	0.53	0.09	0.90	2.01	0.45	0.17	0.48	0.14	1.22	2.42	0.61	0.84	0.91	2.41	0.53	0.08	0.44	0.05
Er	1.05	0.38	1.93	2.27	n.d.	n.d.	2.90	6.51	1.55	0.31	2.71	5.75	1.45	0.57	1.49	0.47	3.24	6.70	1.84	2.28	2.69	6.54	1.55	0.23	1.39	0.14
Tm	0.17	0.07	0.28	0.30	n.d.	n.d.	0.42	0.91	0.24	0.05	0.38	0.76	0.22	0.09	0.23	0.08	0.48	0.90	0.27	0.29	0.40	0.92	0.25	0.05	0.22	0.02
Yb	1.27	0.49	2.07	1.85	n.d.	n.d.	2.77	5.48	1.71	0.20	2.68	4.92	1.64	0.67	1.67	0.56	3.47	5.88	1.94	1.72	2.69	5.58	1.81	0.29	1.59	0.15
Lu	0.20	0.08	0.32	0.24	n.d.	n.d.	0.40	0.73	0.28	0.05	0.39	0.62	0.27	0.10	0.27	0.08	0.50	0.78	0.29	0.22	0.39	0.70	0.30	0.05	0.26	0.02
Hf	2.10	0.78	3.02	0.90	n.d.	n.d.	2.78	1.42	2.77	0.24	3.66	0.90	3.75	1.32	3.71	1.35	3.98	1.15	2.42	0.79	3.67	0.53	4.18	0.59	2.62	0.18
Ta	1.02	0.39	1.37	0.40	n.d.	n.d.	1.05	0.33	1.29	0.05	1.03	0.13	1.07	0.37	1.12	0.34	1.10	0.28	1.10	0.27	1.09	0.13	1.20	0.16	1.28	0.07
Pb	13.61	4.87	18.04	5.41	n.d.	n.d.	14.57	5.22	18.01	1.18	15.16	3.56	15.17	5.35	15.53	5.02	14.45	4.85	16.26	7.27	16.45	3.15	16.81	2.60	17.15	0.86
Th	17.85	6.91	23.58	8.49	n.d.	n.d.	16.93	7.28	22.30	1.31	16.21	4.41	17.61	6.28	18.22	6.54	17.11	6.99	18.69	5.94	17.62	3.78	19.90	2.68	22.46	0.90
U	6.06	2.45	7.79	2.81	n.d.	n.d.	5.57	2.43	7.55	0.53	5.65	1.49	5.95	2.14	6.18	2.21	5.88	2.06	6.30	2.00	6.11	1.23	6.95	1.47	7.35	0.29

n.d., No data.

of these deposits to serve as regional stratigraphic horizon markers for archaeological, palaeoceanographic and palaeoclimatic studies. Specifically, we re-examine the reported southward dispersal of the S1 tephra layer (traced over >1300 km; Fig. 1(a)) and the northward transport of the BSC_079 layer (~500 km), in order to evaluate their geochemical and chronological consistency with proximal Karagüllü, Perikartin and Dikkartin deposits. Ultimately, these integrated correlations provide a framework not only for improving regional tephrochronology but also for refining future volcanic-hazard assessments in Central Anatolia and adjacent regions.

METHODS

Fieldwork: Volcano stratigraphy and sampling

Proximal pyroclastic deposits of Karagüllü, Perikartin and Dikkartin were sampled during a fieldwork campaign conducted in November 2021 for subsequent laboratory-based glass chemical characterisation. Fresh pumice clasts were collected from each tuff ring and sequentially labelled with the prefix 'PSK' (see the sample location in Fig. 1(c) and Doc. S1). Using satellite imagery and published geological maps (e.g., Friedrichs et al., 2020), we targeted well-exposed pyroclastic deposits on and around Erciyes.

A key outcrop on the northern flank of the volcano (Hacilar site; PSK-31/40 in Fig. 1(c) and profile A–A′ in Fig. 1(d)) was studied in detail, as it records numerous tephra layers. Stratigraphic relationships at this site were logged (Fig. 2), and individual tephra layers were described and sampled for glass chemical analyses. For each tephra bed, fresh pumice clasts were collected across the exposed thickness (including lower, middle and upper portions) to capture potential vertical compositional variability. Pumices from the same stratigraphic bed were subsequently combined to obtain a representative sample for geochemical analyses.

Two additional fieldwork campaigns were carried out in June 2022 and May 2023, focused on refining the proximal stratigraphy and contextualising the geochemical and geochronological framework of the studied eruptive deposits. For example, a carbon-rich palaeosol identified at the base of the Hacilar sequence (PSK-31) was collected for radiocarbon dating.

Glass geochemical microanalyses

Lapilli-sized pumices sampled from both the (i) proximal pyroclastic deposits of each tuff ring, Karagüllü, Perikartin and Dikkartin; and (ii) Hacilar site tephra layers, were cleaned, crushed, washed, sieved and dried at the Laboratory of Experimental Volcanology and Geophysics (HP-HT Lab) of the Istituto Nazionale di Geofisica e Vulcanologia (INGV) in Rome, Italy. Glass shards >63 μm were mounted in epoxy resin, polished and carbon-coated for subsequent major and trace element analyses.

Major element compositions of volcanic glass were determined for ~30 shards per sample using a JEOL JXA-8200 electron probe micro-analyser (EPMA) equipped with five wavelength-dispersive spectrometers (WDSs) and installed at the HP-HT Lab of INGV. Analyses were performed under high-vacuum conditions using a 15 kV accelerating voltage, 7.5 nA electron beam current and a 10 μm defocused beam. Elemental counting times were 10 s on peaks and 5 s on background positions. The ZAF (Z: atomic number; A: absorption; and F: fluorescence) correction procedure was applied to account for inter-elemental effects. Calibration used certified standards from micro-analysis consultants (MAC): albite (Si-PET, Al-TAP and Na-TAP), forsterite (Mg-TAP), augite (Fe-LIF), apatite (Ca-PET and P-TAP), orthoclase (K-PET), rutile (Ti-PET) and rhodonite (Mn-LIF). To avoid alkali migration, Na and K were measured first. Quality control was conducted using the Smithsonian rhyolite standard VG-568 (Jarosewich, 2002). Accuracy was better than 1%–5% for most elements (and 5%–10% for elements below 1 wt.%), with precision generally better than 1%–5%.

Trace element compositions were obtained using a 193 nm excimer laser coupled with a two-volume constant geometry ablation cell (Resonetics S-155LR) and a high-sensitivity, laser ablation-inductively coupled plasma mass spectrometer (LA-ICP-MS; Thermo-Element XR) at the Institute of Geochemistry and Petrology of the ETH Zürich (Switzerland). Laser spots (20 μm diameter) were ablated on representative glass shards for 30 s using a pulse rate of 5 Hz and an energy density of ~3.5 J/cm^2. Calibration and instrumental drift correction were performed using the synthetic glass NIST SRM610 (Jochum et al., 2011). Reproducibility was assessed by performing repeated measurements of the GSD-1G (Guillong et al., 2005) and BCR-2G (Raczek et al., 2001) glass reference materials (Doc. S1). Raw data were processed using Iolite 4 (Woodhead et al., 2007; Paton et al., 2010), with ^{29}Si used as the internal standard. The precision of individual analyses varied depending on several factors, including the element and isotope analysed, as well as the homogeneity of the ablated material. The 1σ errors obtained from variations in replicate analyses were invariably several times larger than the fully integrated 1σ errors determined solely from counting statistics.

In addition to the proximal and Hacilar tephra samples, we analysed the BSC_079 cryptotephra layer identified by Cullen et al. (2014) in sediment core M72/5-25-GC1 (Black Sea, Site 1 in Fig. 1(a)) for major and trace element glass compositions to enable a detailed comparison (Table 2). While Cullen et al. (2014) reported major element data and proposed tentative correlations between BSC_079 and either the Perikartin or Karagüllü eruptions, the absence of trace elements limited the robustness of this tephrochronological attribution. Published glass geochemical data from distal tephra layers were also used for comparison with the new proximal and BSC_079 data sets generated in this study. Data for the Lake Brazi cryptotephra (TDB_575) were sourced from Kearney et al. (2024), while glass compositional data for the S1 tephra from the Eastern Mediterranean (samples SL112-260 and SL114-39) were taken from Friedrichs et al. (2020). These data sets are based on electron microprobe and, where available, laser ablation measurements of volcanic glass shards, and are directly comparable with our glass compositions in terms of analytical methodology, major element normalisation procedures and data processing protocols. No additional geochemical analyses of distal tephra samples from Lake Brazi or the Eastern Mediterranean were conducted as part of this study.

Radiocarbon dating

Charred organic material was identified in a well-preserved palaeosol within the Hacılar section. Small fragments of carbonised grass (sample PSK-31; Doc. S2) were sampled in order to obtain a date for a position in the sequence. It was analysed by Beta Analytic Inc. (Miami, FL, USA) using Accelerator Mass Spectrometry (AMS) radiocarbon dating. A standard acid–base–acid (ABA) pre-treatment was applied to remove any potential contamination caused by carbonate and humic acid. The δ^{13}C value was determined by isotope ratio mass spectrometry (IRMS) and used for isotopic fractionation correction. Analyses were performed in-house using four NEC

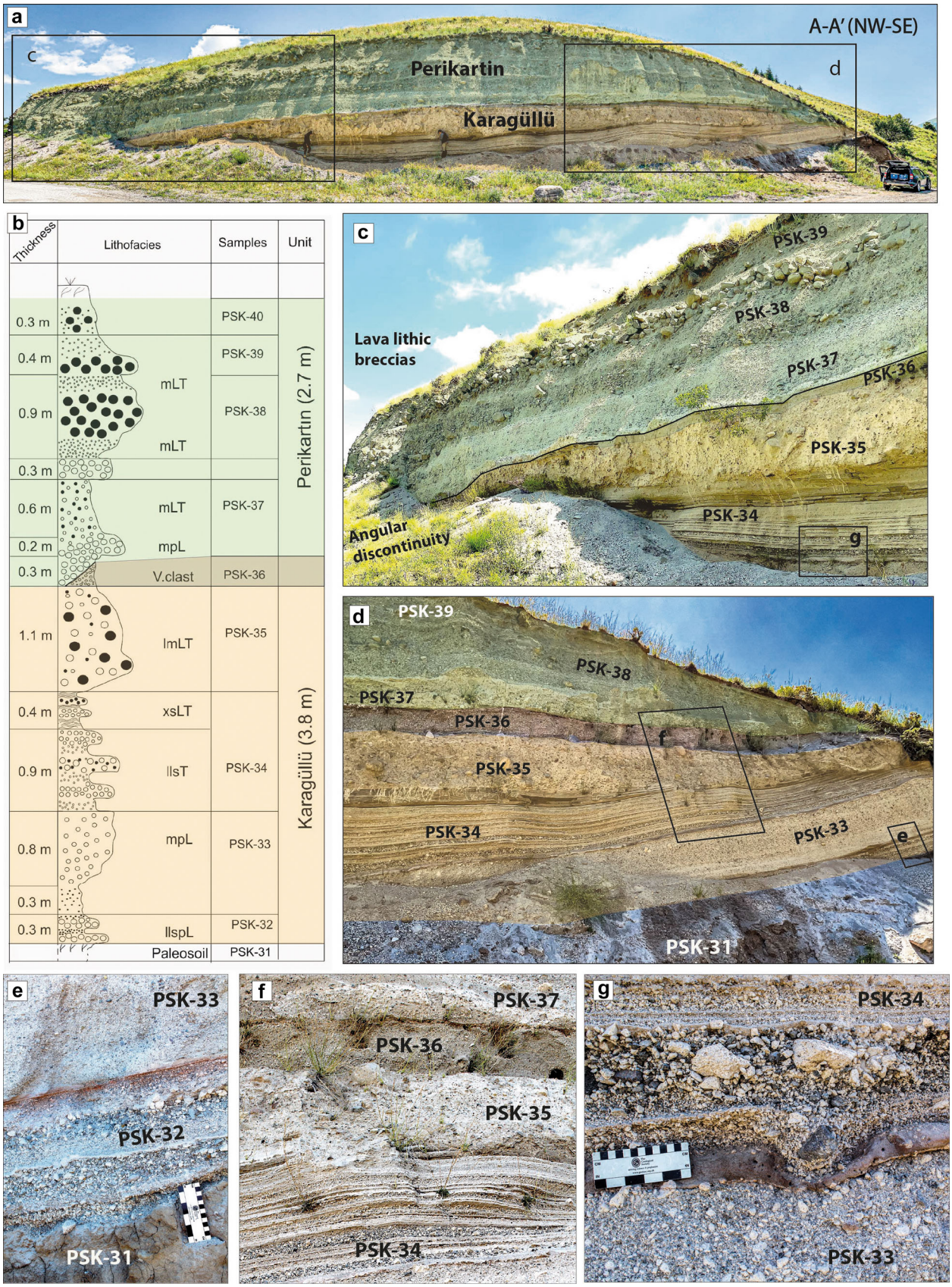

Figure 2. Deposits and stratigraphy exposed at the Hacilar site (coloured overlays are used to distinguish the eruptive units, Karagüllü in orange and Perikartin in green). (a) Panoramic view of the entire outcrop showing the lateral continuity of the Perikartin layers above Karagüllü ones. (b) Composite stratigraphic log of the Hacilar pyroclastic sequence, with thickness, lithofacies sampled tephra layers (PSK-32 to PSK-39) and eruptive units indicated. (c) Close-up view of the lava lithic breccias within the uppermost units of Perikartin, which are atop an angular discontinuity between the above Karagüllü units (NW end of the Hacilar outcrop). (d) Close-up view of the whole Hacilar sequence above the palaeosol (PSK-31)—SE end of the Hacilar outcrop. (e) Detailed view of the pumice fall layers (PSK-32) at the beginning of Karagüllü eruption above a palaeosol. (f) Detailed view of the reworked volcanoclastic materials (PSK-36) between Karagüllü top units (PSK-34 and 35) and Perikartin bottom units (PSK-37). (g) Bomb sags structures generated by ductile deformation of wet ash deposits from ballistic impacts during the phreatomagmatic eruption of the Karagüllü tuff ring. [Color figure can be viewed at wileyonlinelibrary.com]

AMS and four Thermo IRMS units under ISO/IEC 17025:2017 accreditation (PJLA#59423).

The radiocarbon age was calibrated using the IntCal20 calibration curve (Reimer et al., 2020) and the high probability density (HPD) method (Bronk Ramsey, 2009). Analytical accuracy was confirmed through quality assurance protocols using certified reference materials (Doc. S3).

RESULTS

Tephrostratigraphy of the Hacilar site

The Hacilar outcrop exposes a well-preserved ~7-m-thick pyroclastic sequence (Fig. 2), clearly visible along a roadcut on the northern flank of Mount Erciyes (profile A–A′ in Fig. 1(d)). This section lies within a valley downslope from the Perikartin lava dome (38.628689° N, 35.463408° E), which is on the same flank of the volcano as the Karagüllü tuff ring, and it is a key site to investigate the stratigraphic relationships of the pyroclastic deposits associated with Holocene explosive eruptions. The succession comprises multiple, laterally continuous volcanic layers with variable grain sizes and internal structures, including both massive and well-bedded units. Here, we present the results of stratigraphic logging, glass chemical analyses and radiocarbon dating.

Lithofacies and stratigraphy of the Hacilar deposits

In general, the lower part of the section features finely laminated ash beds and pumice-rich layers, overlain by thicker, massive deposits of coarse pumice and lithic fragments (Fig. 2(a)). The base of the section is a dark to reddish–brown, massive, clay-rich horizon characterised by a blocky structure, abundant fine cracks and a clear pedogenic texture (PSK-31; Fig. 2(d),(e)), which is interpreted as a palaeosol. It contains scattered, millimetric fragments of charcoal and carbonised herbaceous material (Doc. S2), which has been used to obtain a radiocarbon age (Section 3.1.3). Above this palaeosol, the Hacilar pyroclastic sequence starts with a 30 cm stratified deposit composed of clast-supported, lithic-rich, fine- to coarse-pumice lapilli layers interbedded with fine ash levels (PSK-32; llspL in Fig. 2(b)–(e)). On top of these finely laminated layers, a sharp, erosional contact marks the base of the overlying 80-cm-thick, massive, poorly sorted lapilli tuff (PSK-33; mLT, Fig. 2(b)–(e)), which contains subangular to subrounded coarse pumice and lithic fragments within a fine ash matrix. The massive bed grades upward into a horizontally stratified sequence of thin, parallel ash and pumice lapilli layers (PSK-34, llsLT & pL, Fig. 2(b)–(d),(f)). The 130-cm-thick stratified deposit shows uniform thickness and lateral continuity, also displaying ductile deformation structures, such as local lens-shaped convolutions beneath larger blocks of pumice or denser lava lithics (Fig. 2(g)). Overlying this interval is another massive deposit (PSK-35), texturally and compositionally similar to the lower massive unit (PSK-33), though slightly coarser in pumice clasts and richer in lithics (PSK-35, lmLT, Fig. 2(b)–(d),(f)). This yellowish unit is followed by a distinctive, tabular, dark brown layer (PSK-36, Fig. 2(b),(d),(f)) with a moderately sorted, bimodal texture. The layer is nearly clast-supported and comprises predominantly medium lapilli-sized, subrounded pumice and smaller lithic clasts within a clay-rich fine ash matrix. Laterally, this 30-cm-thick tabular layer thins progressively towards the northwest end of the outcrop, where it eventually disappears, and the overlying units rest directly atop an angular discontinuity (Fig. 2(a)–(c)).

Above the angular contact, the overlying deposits start with an 80-cm-thick unit of light grey, moderately indurated, pumice-rich massive lapilli tuff (PSK-37), which grades into a 2-m-thick, dark grey, stratified deposit rich in lithics and matrix of fine ash (PSK-38 and 39; Fig. 2(a)–(d)). This bedset is increasingly enriched in subrounded lava blocks towards the northeastern end of the outcrop, where these fragments accumulate to form lithic breccias. Lapilli clasts are subangular to subrounded and range from fine to coarse lapilli in size. This upper section appears laterally continuous across the outcrop and maintains a consistent thickness, although it displays variable facies expressions of the same eruptive unit.

Glass geochemistry

To support the volcano-stratigraphic study at Hacilar site, major and trace element data of tephra layers PSK-32 to PSK-39 (Fig. 2) are shown on the TAS (total alkali vs. silica) diagram, major trace element variation plots and multi-element spider diagrams (Fig. 3). These data were compared to the glass compositional fields of Karagüllü (made by PSK-43 plots), Perikartin (PSK-41) and Dikkartin (PSK-48) proximal deposits (Fig. 3) to assign each Hacilar layer to its corresponding eruption. Average concentrations and standard deviations for each analysed major and trace element are presented in Table 2, while the complete data set is provided in Doc. S1.

All deposits are rhyolitic in composition, with 74–78 wt.% SiO_2 and a total alkali content of ~6.5–9 wt.% ($Na_2O + K_2O$; Fig. 3(a)). However, the tephra units show varying degrees of magmatic evolution. The lowermost Hacilar units (PSK-32 to PSK-36) are the most evolved, with higher SiO_2, and lower CaO and FeO_t compared to the overlying deposits (Fig. 3(b),(c); Table 2). Most glass analyses from these basal units, extending from the bottom of the sequence up to the angular discontinuity, overlap with the pyroclastic deposits of Karagüllü eruption, including their trace element contents (Fig. 3(d),(e)). In contrast, the upper Hacilar units (from PSK-37 to PSK-39), located above the angular discontinuity up to the top of the sequence (Fig. 2), are slightly less evolved (Fig. 3(a)–(c)). These share the same major and trace element glass composition as both the Perikartin and Dikkartin eruption deposits.

Radiocarbon dating

Radiocarbon analysis of the carbonised grass fragments sampled from beneath the Hacilar pyroclastic sequence (PSK-31 in Fig. 2) yielded a conventional radiocarbon age of 9850 ± 30 yr BP (Beta-680269), corresponding to a calibrated age range of 9366–9253 cal BC at 95.4% probability. This places the formation and burial of the palaeosol in the early Holocene, between 11 315 and 11 202 cal yr BP, at 95.4% probability (11 258 ± 56 cal yr BP; Fig. 4). The measured $\delta^{13}C$ value (−24.6‰) is consistent with terrestrial C_3 plant material, supporting its reliability for accurate radiocarbon dating.

Chemical composition of BSC_079 tephra

Cullen et al. (2014) proposed a possible correlation of the BSC_079 tephra layer in the Black Sea sediment core (M72/5-25-GC1) with either the Karagüllü or Perikartin eruptions of Mount Erciyes. However, the absence of trace element data prevented a definitive attribution. To resolve the origin of the BSC_079, we re-analysed 100 individual glass shards (Fig. 5), focusing not only on major elements but also on performing trace element analyses for the first time. The average concentrations and standard deviations for each

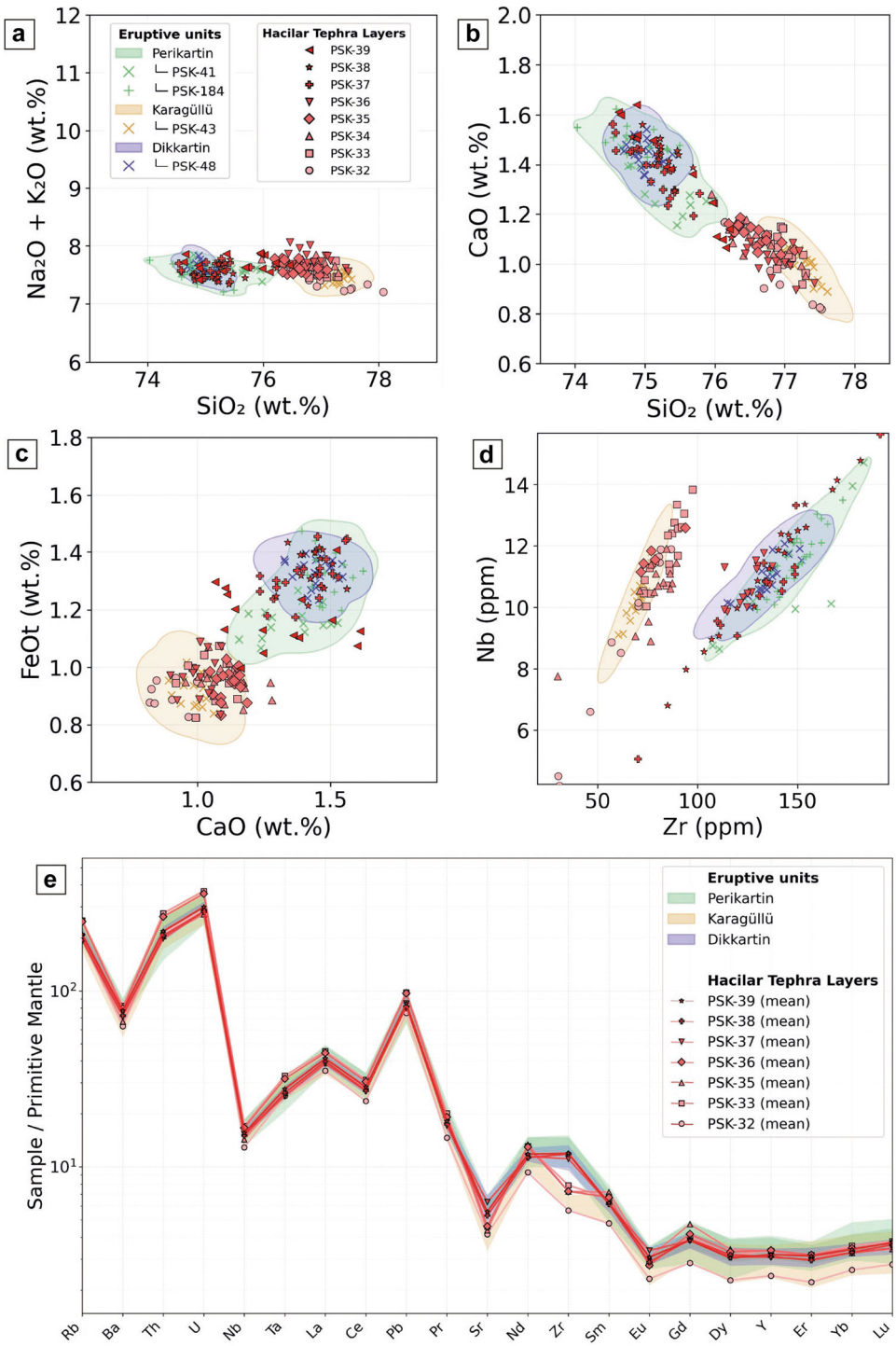

Figure 3. (a) TAS (total alkali vs. silica) diagram showing that all Hacilar tephra layers are rhyolitic and fall within the Karagüllü, Perikartin and Dikkartin compositional fields; (b) CaO versus SiO_2 diagram; (c) FeO versus CaO diagram; (d) Nb versus Zr diagram; (e) Primitive mantle-normalised spider diagram showing the trace element concentrations of all Hacilar tephra layers. The patterns are broadly similar and consistent with a cogenetic magma evolution leading to enrichment in large-ion lithophile elements (LILE: Rb, Ba and Th) and negative anomalies in Sr and Eu, typical of more differentiated calc-alkaline rhyolitic magmas. [Color figure can be viewed at wileyonlinelibrary.com]

analysed major and trace element are presented in Table 2, while the complete data set is provided in Doc. S1.

Major element compositions confirm the rhyolitic nature of BSC_079, consistent with the findings of Cullen et al. (2014), and place it within the compositional field of Karagüllü eruption (Fig. 6(a)). More significantly, the trace element signature of BSC_079 closely resembles that of proximal Karagüllü deposits, particularly in terms of Zr, Nb and rare earth element (REE) concentrations (Fig. 6(b),(c)), and differs from the compositions of Perikartin and Dikkartin. Importantly, BSC_079 data display tight grouping, low dispersion and strong internal geochemical coherence, including pronounced negative anomalies in Sr and Eu and flat to slightly declining heavy rare earth elements (HREE) patterns.

DISCUSSION

Volcanic products and sedimentary processes recorded at the Hacilar site

The lowermost pyroclastic units at the Hacilar site, deposited above a palaeosol dated to 11 258 ± 56 cal yr BP (Fig. 4), are

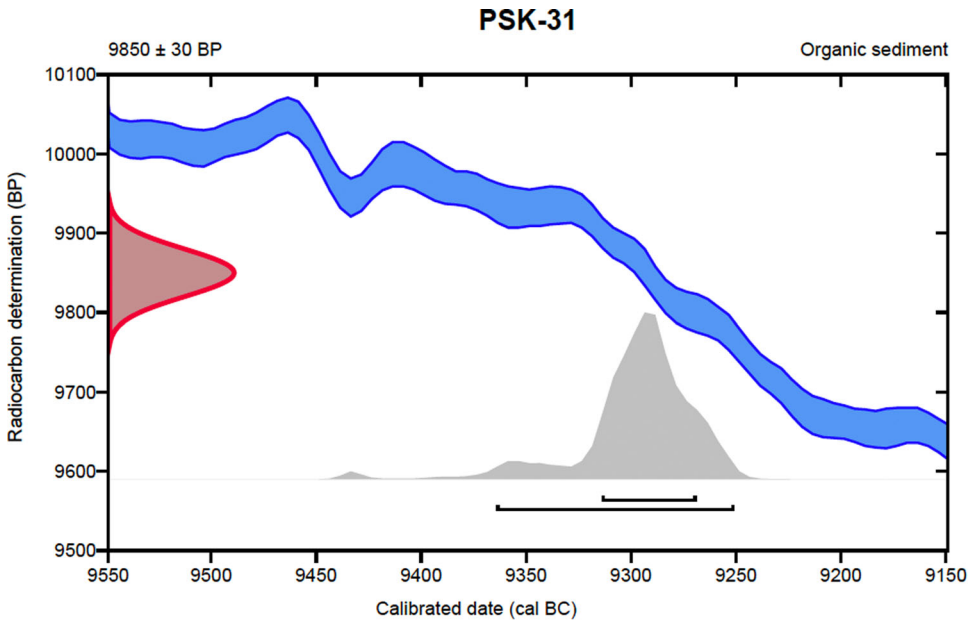

Figure 4. Radiocarbon calibration curve and calibrated age range for sample PSK-31, collected from the palaeosol directly underlying the Karagüllü pyroclastic sequence at the Hacılar site. The red curve on the left represents the probability distribution of the uncalibrated conventional radiocarbon age (9850 ± 30 yr BP). The blue band shows the IntCal20 calibration curve with its associated 2σ uncertainty range. The grey area represents the calibrated probability distribution, with two horizontal black bars indicating the 68.2% (9316–9271 cal BC) and 95.4% (9366–9253 cal BC) confidence intervals (corresponding to 11 258 ± 56 cal yr BP at 95.4% probability). Calibration was performed using OxCal v4.4 and the IntCal20 data set (Reimer et al., 2020). [Color figure can be viewed at wileyonlinelibrary.com]

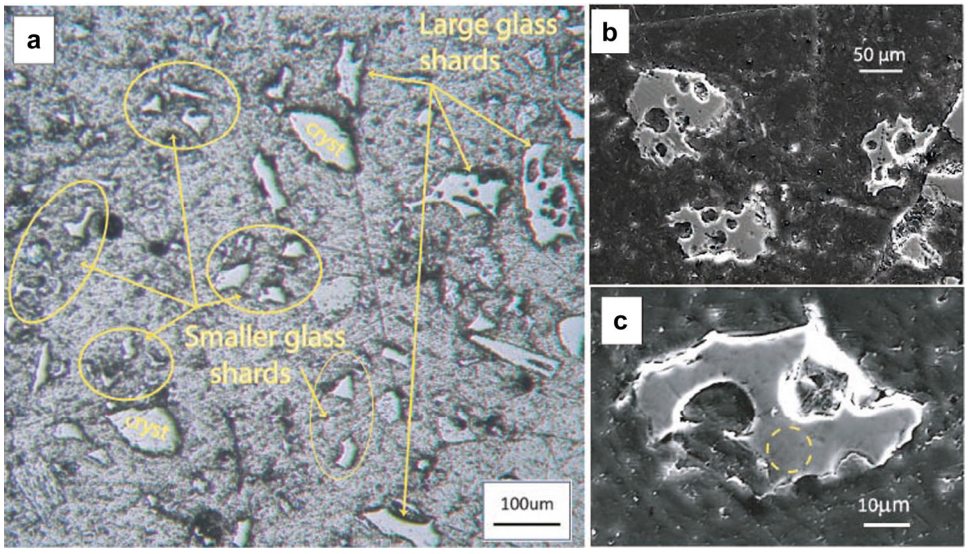

Figure 5. Microphotographs of the BSC_079 tephra layer. (a) Petrographic microscope images showing a great number of glass shards with variable sizes (e.g., pumiceous type up to 100 µm); (b) Back-scattered electron (BSE) image showing vesicular glass shards with irregular morphologies; (c) Close-up BSE image of a single, highly vesiculated glass shard showing thin bubble walls and cuspate edges, indicative of explosive fragmentation (note the 10 µm pit, as indicated by the yellow dashed circle). [Color figure can be viewed at wileyonlinelibrary.com]

attributed to the Karagüllü eruption based on the stratigraphy (Fig. 2), the outcrop location (Fig. 1(c),(d)) and its chemical composition (Fig. 3). This radiocarbon date constrains the age of the palaeosurface immediately before the eruption of the Karagüllü pyroclastic deposit. The sharp and undisturbed stratigraphic contact between them indicates primary deposition, and therefore dates the associated eruption. At this outcrop, the Karagüllü products begin with a characteristic tuff ring sequence, comprising phreatomagmatic dilute surges interbedded with pulsatory pumice fallout layers (stratified PSK-32, Fig. 2(e)), with bomb sag structures (PSK-34, Fig. 2(g)). This sequence is interrupted twice by massive, rapidly emplaced, dry and more energetic pyroclastic density currents (PDCs, PSK-33 and PSK-35; Fig. 2(a)–(f)). At the top of the Karagüllü sequence, the PDC unit becomes thicker and more lithic-rich, partially eroding the underlying phreatomagmatic sequence (PSK-34; Fig. 2(c),(d),(f)). These units are interpreted to reflect transient changes in eruptive dynamics associated with instability of the growing tuff-ring edifice, as indicated by their massive character, higher lithic content and locally erosive basal contacts. Both the stratigraphic relationships and the glass geochemistry support this interpretation, with samples PSK-33 to PSK-35 plotting within the Karagüllü compositional field (Fig. 3).

At the northwestern end of the Hacilar site, the upper part of the Karagüllü deposit is eroded (PSK-35, Fig. 2(c)), whereas the southeastern end is overlain by reworked volcanoclastic material (Fig. 2(d)) derived from the Karagüllü deposit itself

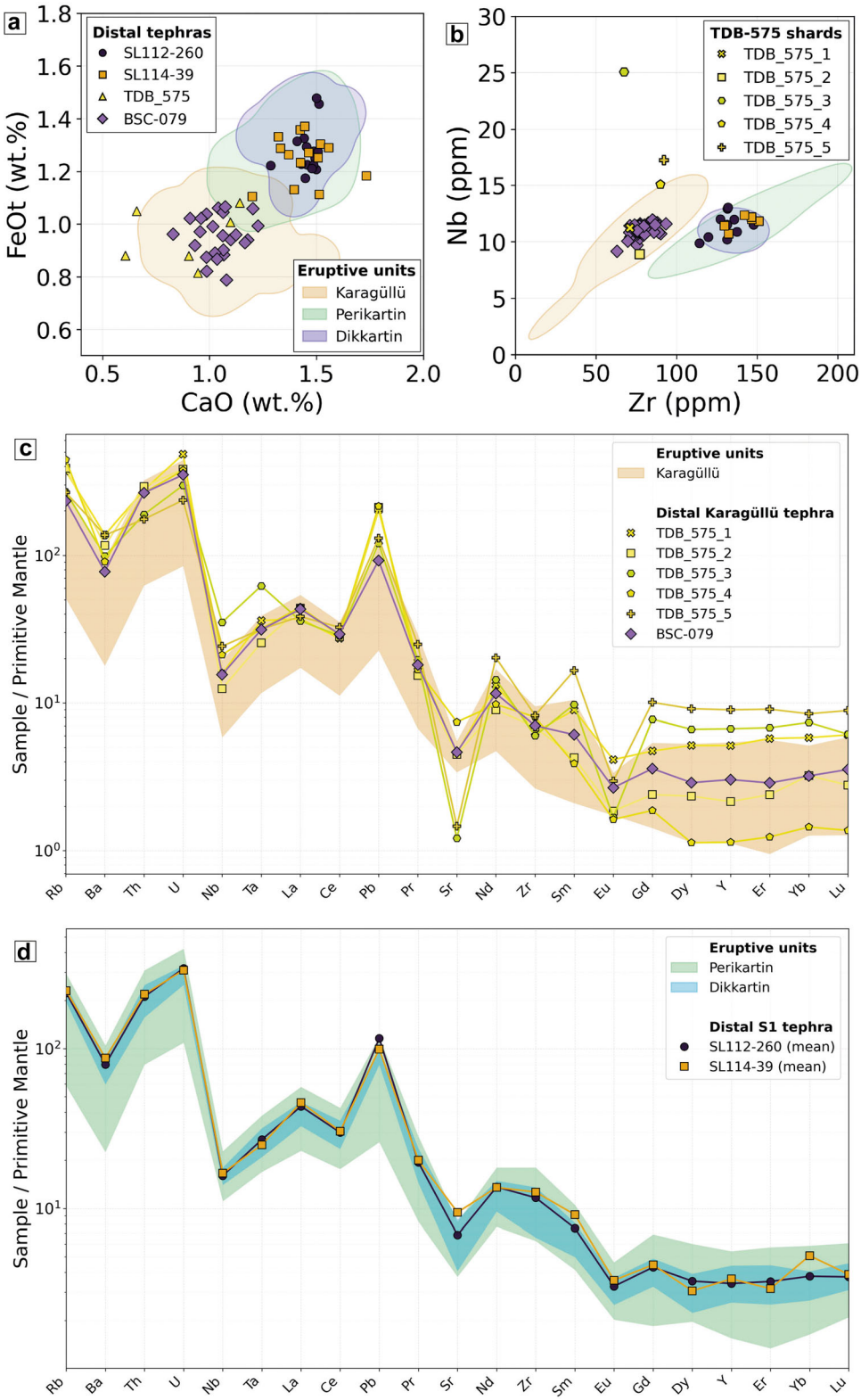

Figure 6. Major and trace element compositions of the distal tephra layers are compared to those of the glass shards from the three Holocene Erciyes eruptions (including the proximal tuff ring samples and the Hacilar pyroclastic deposits). (a) CaO versus FeOt diagram; (b) Zr versus Nb diagram. These diagrams show the distribution of glass compositions from the distal tephra layers BSC_079 (Black Sea; this study), TDB_575 (Brazi Lake; data from Kearney et al. 2024) and SL112-260 and SL114-39 (Eastern Mediterranean; data from Friedrichs et al., 2020), in relation to the compositional fields of the proximal Karagüllü, Perikartin and Dikkartin deposits. (c) Primitive mantle-normalised spider diagrams using the mean value of the BSC_079 microanalyses and the five glass shards of TDB_575 (Kearney et al. 2024) that were successfully analysed by laser ablation to measure the trace elements' concentrations; (d) Primitive mantle-normalised spider diagrams of the distal tephras SL112-260 and SL114-39 (Friedrichs et al., 2020). Both spider diagrams show enrichment in large ion lithophile elements (e.g., Rb, Ba and Th), depletion in Sr and Eu, consistent patterns among BSC_079 and TDB_575 with the Karagüllü fingerprint. Shaded envelopes represent 1σ analytical error. [Color figure can be viewed at wileyonlinelibrary.com]

(see the composition of sample PSK-36 in Fig. 3). The chemistry, colour and texture of this tabular layer collectively suggest post-depositional and limited sedimentary reworking. On the opposite side of the valley, just in front of the Hacilar site, a thick palaeosol is observed directly above the Karagüllü products (Doc. S2), further supporting the existence of a stratigraphic hiatus. In particular, these sedimentary structures (i.e., angular discontinuity, reworked deposits and a palaeosol) indicate a significant time gap between the deposition of the lowermost and the uppermost pyroclastic units at the Hacilar site, corresponding to a period of quiescence between two separate eruptions.

Stratigraphic relationships (Fig. 2), outcrop location (Fig. 1(c),(d)) and glass chemistry (Fig. 3) indicate that the pyroclastic deposits overlying the Karagüllü units at the Hacilar site derive from the ~9.8 ka Perikartin eruption. The uppermost levels are rich in lithic clasts, particularly the breccias shown in Fig. 2(a),(c). We interpret these layers as the product of voluminous PDCs generated by gravitational collapse during partial destruction of the Perikartin tuff ring as its lava dome extruded (Fig. 1(d)). This interpretation is supported by the fact that Hacilar lies along a gully originating just north of the Perikartin dome, which cuts across the Perikartin ring and channels its deposits downslope (Fig. 1(d)). Consistently, no evidence of Dikkartin-derived products is found at Hacilar, as the Erciyes central crater acted as a topographic barrier preventing any lithic-rich PDCs from the southern flank from reaching this northern site.

Correlating distal tephras with Erciyes Holocene eruptions

The new geochemical data set presented in this study confirms that the BSC_079 cryptotephra found in a Black Sea sediment core (Cullen et al., 2014) is the distal ash fallout of the Karagüllü eruption (Fig. 6(a)–(c)). As modelled by Nowaczyk et al. (2012), the age of the cryptotephra position in the Black Sea core is ~13 cal ka BP, which is more compatible with our new radiocarbon dating of the proximal Karagüllü deposits at the Hacilar site (i.e., ~11.3 cal ka BP palaeosol; Fig. 4) than with the younger Perikartin age (~9.8 ka; Sarikaya et al., 2019). It is therefore likely that winds blowing during the Early Holocene Erciyes eruption transported the Karagüllü tephra cloud northward, reaching the Turkish coastline of the Black Sea (star 1 in map of Fig. 1(a)). Cullen et al. (2014) counted at least 53 000 glass shards per gram of sediment within the BSC_079 layer. We estimate that this shard concentration corresponds to approximately ~0.8 mm of ash deposition, as the Campanian Ignimbrite (BSC_721) forms a visible ~1 mm layer in the core and has shard concentrations of ~67 000 shards/gram (Cullen et al., 2014; Cullen, 2015).

Additionally, we compared the major and trace element glass compositions from a cryptotephra layer identified in Lake Brazi (Romania; TDB_575; Kearney et al., 2024), dated to ~13.2 cal ka BP. Several analysed glass shards plot within or close to the Karagüllü compositional field in major and trace element diagrams (Fig. 6(a)–(c)). Although the limited number of analysed shards and uncertainties related to the distal depositional context preclude a firm correlation with Karagüllü eruption, this observation is consistent with the capacity of Erciyes volcano to disperse ash towards continental Europe during the Late Pleistocene–Early Holocene transition. We also compared the glass compositions of the S1 tephra layer preserved in the Eastern Mediterranean, using samples SL112-260 and SL114-39 from sediment cores in the Levantine Sea (Schmidt, 2007; Hamann et al., 2010) and analysed by Friedrichs et al. (2020). These two samples show nearly identical major and trace element compositions (Fig. 6(a),(b),(d)), characterised by enrichment in large ion lithophile elements (e.g., Rb, Ba and Th) and depletion in Sr and Eu. Their geochemical signatures closely match those of the proximal deposits of Perikartin and Dikkartin tuff rings (Fig. 6), supporting previous interpretations that correlate the widespread S1 tephra with explosive eruptions of Erciyes (e.g., Hamann et al., 2010; Neugebauer et al., 2017; Friedrichs et al., 2020), as further discussed in Section 4.3.

Chronologically, the S1 tephra is consistently dated to ~9 cal ka BP across multiple Eastern Mediterranean and Levantine sedimentary records (Develle et al., 2009; Hamann et al., 2010; Neugebauer et al., 2017). This age coincides with the timing of the Dikkartin eruption, independently constrained at ~9.0 ± 0.6 cal ka BP (Friedrichs et al., 2020) via double-zircon dating, whereas the Perikartin eruption is slightly older, at 9.7 ± 0.1 cal ka BP (Sarikaya et al., 2019). Dispersal reconstructions further indicate that the S1 tephra was transported predominantly southwards from Central Anatolia towards the Eastern Mediterranean, consistent with the large magnitude and Plinian-style dynamics inferred for the Dikkartin eruption (Ersoy et al., 2019).

Considering the close geochemical affinity of S1 with both Perikartin and Dikkartin deposits, the overlapping yet closer temporal alignment with Dikkartin and the substantially greater eruptive magnitude and dispersal potential of the Dikkartin Plinian event, we interpret the S1 tephra primarily as distal fallout from the Dikkartin eruption. Nevertheless, given the near-identical glass chemistry of the two tuff-ring deposits, we cannot exclude the possibility that Perikartin and Dikkartin tapped a common magma system and erupted within a relatively short time interval, such that the S1 layer may locally incorporate contributions from both eruptions. This scenario is consistent with a single eruptive phase expressed through multiple vents, although the available data do not yet allow this to be demonstrated unequivocally.

Building upon the distal–proximal tephrochronological correlations established above, we next integrate these constraints to reconstruct the relative chronology and sequence of Holocene explosive eruptions at Erciyes volcano.

Reconstructing the eruptive history of the Erciyes Holocene tuff rings

Based on the tephrostratigraphic study conducted at the Hacilar site, we highlight that the Karagüllü eruption represents the earliest and an independent Holocene eruptive event of Erciyes volcano. A new radiocarbon age obtained from charred grass fragments preserved in a palaeosol directly beneath the Karagüllü pumice fallout provides a robust chronological constraint, dating the eruption to shortly after 11 200 cal yr BP (Fig. 4; see also Doc. S2 and S3). The excellent preservation of the carbonised vegetation and the sharp stratigraphic contact between the palaeosol and the overlying pyroclastic deposits (Fig. 2(d),(e)) confirm a primary depositional setting and reinforce the reliability of the dated horizon. It is most likely that the hot pumice fallout deposited during the initial stages of the Karagüllü tuff ring eruption buried and carbonised the live vegetation growing on the palaeosurface.

The eruption chronology of the three Holocene tuff rings of Erciyes volcano is summarised in Fig. 7, integrating our new radiocarbon result for the Karagüllü eruption with previously published (U-Th)/He zircon ages, cosmogenic ^{36}Cl surface exposure ages and radiocarbon datings from proximal Perikartin and distal S1 tephra records (modified after Friedrichs et al., 2020). The coloured bars in Fig. 7 represent

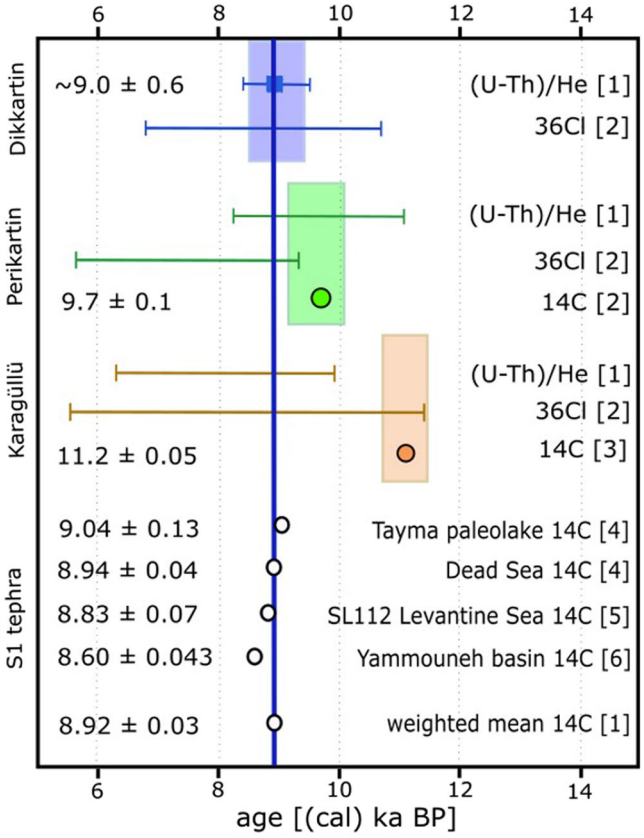

Figure 7. Chronogram of the Holocene Erciyes tuff ring eruptions modified after Friedrichs et al. (2020). The chronogram integrates the radiocarbon ^{14}C age of Karagüllü eruption presented in this study [3, orange circle] along with published geochronological data indicated by coloured bars: the [1] zircons (U–Th)/He ages (Friedrichs et al., 2020, 2021) and [2] cosmogenic ^{36}Cl lava surface for the three domes (Sarikaya et al., 2019). The green circle indicates the radiocarbon ^{14}C age reported by Sarikaya et al. (2019) for Perikartin PDCs [2]. The white circles indicate radiocarbon ages of S1 tephra measured in [4] Tayma palaeolake and Dead Sea (Neugebauer et al., 2017), [5] Levantine Sea (Hamann et al., 2010) and [6] Yammouneh basin (Develle et al., 2009). The coloured shadings (blue, green and orange rectangles) represent our preferred age ranges for each tuff ring eruption, based on the integration of all available geochronological data. [Color figure can be viewed at wileyonlinelibrary.com]

the eruption ages of Karagüllü, Perikartin and Dikkartin derived from different dating techniques (orange, green and blue, respectively). White circles correspond to calibrated radiocarbon ages of the distal S1 tephra measured in various regional archives, including the Tayma palaeolake and Dead Sea (Neugebauer et al., 2017), Levantine Sea (Hamann et al., 2010) and Yammouneh basin (Develle et al., 2009). The chronogram clearly shows that the Karagüllü eruption predates the Perikartin event by approximately 1500 years. The radiocarbon age of 9.7 ± 0.1 cal ka BP for Perikartin, based on a charred tree trunk buried within pyroclastic density current deposits (Sarikaya et al., 2019), is consistent with the geochronological constraints shown in Fig. 7. At Hacılar, the presence of a palaeosol, a reworked volcaniclastic layer and an angular unconformity between Karagüllü and Perikartin deposits further supports a significant stratigraphic hiatus between the two events.

In contrast to Karagüllü and Perikartin, no palaeosol or organic-rich layer was preserved beneath the Dikkartin fallout deposits at the outcrops examined in this study (e.g., PSK-46; Fig. 1(c)), precluding the acquisition of new radiocarbon ages. Consequently, the double-dating U–Th/He ages of ~9.0 ± 0.6 cal ka BP (Friedrichs et al., 2020), derived from juvenile zircons in proximal deposits, represent the sole direct chronological constraint for the Dikkartin eruption. Although these ages are interpreted as eruption ages, their relatively large analytical uncertainties yield a lower temporal resolution compared to that typically attainable by radiocarbon dating of distal tephra layers (Fig. 7), underscoring the necessity of integrating multiple independent chronological proxies.

In this context, and building upon the distal–proximal correlations discussed in Section 4.2, the strong geochemical correspondence between the Dikkartin proximal glass compositions and the widespread S1 tephra detected in Eastern Mediterranean records (e.g., SL112-260 and SL114-39; see Section 4.2 and Fig. 6) provides a critical complementary chronological constraint. The clustering of multiple calibrated radiocarbon ages around ~9 cal ka BP for the S1 tephra in distal marine and lacustrine archives (Fig. 7) supports a close temporal association between S1 deposition and the Dikkartin eruption, suggesting that Dikkartin represents the youngest of the three Holocene explosive eruptions of Erciyes. Nevertheless, given the overlapping age ranges of the Dikkartin and Perikartin deposits, coupled with their nearly identical glass chemistry, we cannot exclude the possibility that both eruptions occurred within a relatively short time interval and jointly contributed to this widespread regional ash layer (i.e., the S1 tephra). Similar patterns have been documented in other silicic volcanic systems characterised by fissure-fed or multi-vent activity, where eruptions of closely related magma batches occurred within short temporal windows (e.g., Ayele et al., 2007; Seropian et al., 2021). Unlike volcanic systems such as Campi Flegrei, where contemporaneous or closely spaced eruptions are documented through interdigitated and compositionally distinct proximal deposits (e.g., Pistolesi et al., 2016), no such stratigraphic relationships are exposed at Erciyes, limiting the ability, based solely on field evidence, to determine whether Perikartin and Dikkartin represent synchronous eruptions or spatially distinct expressions of a single eruptive episode. Addressing this question will require future integrated studies, including geochemical and petrological analyses of eruptive deposits to constrain magma source and storage conditions, structural investigations of potential dike or fissure systems and targeted drilling and high-resolution sediment coring (e.g., within the current ÇoraDrill project) to assess whether proximal-to-medial archives preserve a single composite tephra layer or multiple closely spaced fallout events. Overall, the integration of proximal geochronology and distal tephrochronological records enables a robust constraint on the age of the Dikkartin eruption to ~9 cal ka BP.

Tephra dispersal, implications and hazard assessment

The S1 tephra, derived from the last eruptive event of Erciyes at ~9 cal ka BP, provides compelling evidence that the eruption dispersed ash over distances exceeding 1300 km towards the south and southeast of its eruption vent (Fig. 1(a)) during the Holocene (e.g., Hamann et al., 2010; Neugebauer et al., 2017; Friedrichs et al., 2020). This widespread ash fallout blanketed large areas of the Levantine Sea and the Fertile Crescent, reaching parts of the Middle East, Egypt and the Arabian Peninsula (Fig. 1(a)). Based on the combined tephrostratigraphic, geochemical and geochronological evidence, we confirm the S1 tephra as the product of the Dikkartin eruption. However, given the compositional similarity and partially overlapping ages of the Dikkartin and Perikartin deposits, a contribution from the Perikartin tuff ring cannot be ruled out. If both eruptions were contemporaneous, they could have produced a composite ash layer resulting from dual eruptive activity on opposite flanks of the Erciyes edifice.

The Holocene Erciyes eruptions also dispersed tephra northward for more than 500 km. This is exemplified by the BSC_079 cryptotephra, attributed to the Karagüllü eruption, which was identified in the Black Sea sediment core M72/5-25-GC1 (star 1 in Fig. 1(a)). Furthermore, tephra dispersal may have extended more than 1000 km northwestward, potentially reaching the Balkan Peninsula, as suggested by the TDB_575 tephra layer found in Lake Brazi (Kearney et al., 2024), Romania (star 8 in Fig. 1(a)). The new age reported for the Karagüllü tuff ring (11 258 ± 56 cal yr BP; Fig. 4), along with the associated proximal tephrostratigraphy, redefines the Holocene eruptive chronology of Erciyes volcano. Additionally, due to the widespread dispersal of Karagüllü distal ashes, the BSC_079 tephra may represent a valuable horizon marker in regional studies. For example, the deposition of this tephra layer, as well as the S1 tephra, coincides with a climatically and culturally pivotal period in the eastern Mediterranean region, overlapping with the onset of the warmer early Holocene climate and the Neolithic in nearby areas (e.g., Rossignol-Strick et al., 1982; Hamann et al., 2010; Friedrichs et al., 2020). The availability of a precise absolute age for the Karagüllü eruption thus strengthens the regional tephrochronological framework and enhances its role in palaeoenvironmental reconstructions.

These tephrochronological correlations significantly contribute to improving volcanic hazard assessments in Anatolia and within adjacent regions, including the Mediterranean and south-eastern Europe, which have historically not been considered areas at risk from eruptions of the CAVP. The hypothetical scenario of different tuff rings erupting contemporaneously would imply a more complex eruptive dynamic. Should multi-vent explosive activity at Erciyes be confirmed, volcanic hazards in Central Anatolia would need to be re-assessed accordingly.

CONCLUSIONS

This study refines the Holocene explosive eruptive history of Mount Erciyes through the integration of new proximal tephrostratigraphy and a review of distal tephra correlations. We provide a robust chronological and geochemical characterisation of the Karagüllü, Perikartin and Dikkartin tuff rings. On this basis, two main glass populations are recognised: Karagüllü and Perikartin–Dikkartin. The Karagüllü eruption is confidently dated to ~11 258 cal yr BP here based on a radiocarbon determination from a well-preserved palaeosol, and its products are geochemically correlated with the BSC_079 cryptotephra in the Black Sea, indicating ash dispersal over 500 km north of the eruptive vent. A similar geochemical fingerprint is also observable in previously published glass shard compositions from the TDB-575 cryptotephra layer in Lake Brazi, Romania, more than 1000 km to the northwest. Although only a few shards were identified, and their provenance as primary fallout remains uncertain, this correlation suggests the possibility of a much broader ash dispersal for the Karagüllü eruption.

While the Perikartin eruption has been constrained to ~9.7 cal ka BP in previous studies, the regionally widespread S1 tephra, which is geochemically consistent with the Perikartin–Dikkartin glass population, provides the main chronological constraint for the more voluminous Dikkartin Plinian eruption, placing its age at ~9 cal ka BP. Re-assessment of previously published distal correlations supports this attribution. Nevertheless, considering the overlapping age constraints, the near-identical glass compositions of the Dikkartin and Perikartin deposits, and the lack of direct stratigraphic superposition, it remains plausible that both vents were active within a short time interval, representing spatially distinct expressions of a single eruptive episode rather than strictly independent eruptions.

Our findings strengthen the tephrochronological framework of Central Anatolia Volcanic Province and provide new relevant stratigraphic markers for palaeoenvironmental and archaeological studies across Europe and the Eastern Mediterranean. Crucially, the recognition of >500–1000 km ash dispersal patterns, as documented for the Karagüllü eruption, highlights that even relatively modest-sized eruptions from Anatolian volcanoes can have transcontinental impacts and calls for a re-assessment of regional volcanic hazard scenarios.

Acknowledgements. This work has been funded by the PÜSKÜRÜM project, a Marie Skłodowska-Curie Individual Fellowship awarded to ISP (MSCA grant #101024337) under the European Union's Horizon 2020 research and innovation programme, with additional funding from the Add-Sapiexcellence initiative of Sapienza University of Rome (grant #1715/2024), and the Spanish Ministry of Science, Innovation and Universities under TURVO project PID2023-147255NB-I00, supported by MCIN/AEI (10.13039/501100011033), and co-funded by the European Union–ERDF 'A way of making Europe' (FEDER). This research has also received funding from the Italian National Recovery and Resilience Plan (PNRR), Mission 4 'Education and Research'—Component 2 'From Research to Business'—Investment 1.2 'Funding projects presented by young researchers', within the project ÇoraDrill (CUP B83C25001180001), funded by the European Union—NextGenerationEU. We thank Simge Kaya for fieldwork assistance.

Data availability statement

All data supporting the findings of this study are provided within the supplementary materials (SM1–SM4), which include the complete geochemical and chronological datasets used in this work. These materials will be publicly available upon publication of the article. In addition, the full geochemical (EPMA and LA-ICP-MS glass analyses) and geochronological (radiocarbon) datasets have been deposited in an open-access Zenodo repository (Sunyé-Puchol et al., 2026) and are accessible via https://doi.org/10.5281/zenodo.19065404.

Conflicts of Interest—The authors declare no conflicts of interest.

Supporting information

Additional supporting information can be found in the online version of this article.

Supporting information.

References

Albert, P.G., Hardiman, M., Keller, J., Tomlinson, E.L., Smith, V.C., Bourne, A.J. et al. (2015) Revisiting the Y-3 tephrostratigraphic marker: a new diagnostic glass geochemistry, age estimate, and details on its climatostratigraphical context. *Quaternary Science Reviews*, 118, 105–121. Available from: https://doi.org/10.1016/j.quascirev.2014.04.002

Ayele, A., Jacques, E., Kassim, M., Kidane, T., Omar, A., Tait, S. et al. (2007) The volcano–seismic crisis in Afar, Ethiopia, starting September 2005. *Earth and Planetary Science Letters*, 255, 177–187. Available from: https://doi.org/10.1016/j.epsl.2006.12.014

Barton, R.N.E., Lane, C.S., Albert, P.G., White, D., Collcutt, S.N., Bouzouggar, A. et al. (2015) The role of cryptotephra in refining the chronology of Late Pleistocene human evolution and cultural change in North Africa. *Quaternary Science Reviews*, 118, 151–169. Available from: https://doi.org/10.1016/j.quascirev.2014.09.008

Bronk Ramsey, C. (2009) Bayesian analysis of radiocarbon dates. *Radiocarbon*, 51(1), 337–360. Available from: https://doi.org/10.1017/S0033822200033865

Cullen, V. (2015) *Tephrochronology as a tool for assessing the synchronicity of Middle Palaeolithic and Upper Palaeolithic techno-complexes in the Caucasus* Doctoral dissertation, University of Oxford.

Cullen, V.L., Smith, V.C. & Arz, H.W. (2014) The detailed tephrostratigraphy of a core from the south-east Black Sea spanning the last ~60 ka. *Journal of Quaternary Science*, 29(7), 675–690. Available from: https://doi.org/10.1002/jqs.2739

Develle, A.-L., Williamson, D., Gasse, F. & Walter-Simonnet, A.-V. (2009) Early Holocene volcanic ash fallout in the Yammoûneh lacustrine basin (Lebanon): tephrochronological implications for the Near East. *Journal of Volcanology and Geothermal Research*, 186, 416–425. Available from: https://doi.org/10.1016/j.jvolgeores.2009.07.016

Druitt, T.H., Edwards, L., Mellors, R.M., Pyle, D.M., Sparks, R.S.J., Lanphere, M. et al. (1999) Santorini Volcano. *Memoir of the Geological Society of London*, 19, 176. Available from: https://doi.org/10.1002/esp.205

Ersoy, O., Aydar, E., Şen, E. & Gourgaud, A. (2019) Contrasting fragmentation and transportation dynamics during the emplacement of Dikkartın rhyodacitic dome; Erciyes stratovolcano, central Turkey. *Mediterranean Geoscience Reviews*, 1, 223–242. Available from: https://doi.org/10.1007/s42990-019-00014-4

Friedrichs, B., Atıcı, G., Danišík, M., Yurteri, E. & Schmitt, A.K. (2021) Sequence modeling in zircon double-dating of early Holocene Mt. Erciyes domes (Central Anatolia). *Quaternary Geochronology*, 61, 101129. Available from: https://doi.org/10.1016/j.quageo.2020.101129.

Friedrichs, B., Schindlbeck-Belo, J.C., Danišík, M., Jenkins, S.F., Yurteri, E., Çobankaya, M. et al. (2020) New insights into source and dispersal of Mediterranean S1 tephra, an early Holocene marker horizon erupted at Mt. Erciyes (Turkey). *Quaternary Science Reviews*, 249, 106606. Available from: https://doi.org/10.1016/j.quascirev.2020.106606.

Guillong, M., Hametner, K., Reusser, E., Wilson, S.A. & Günther, D. (2005) Preliminary characterisation of new glass reference materials (GSA-1G, GSC-1G, GSD-1G and GSE-1G) by laser ablation-inductively coupled plasma-mass spectrometry using 193 nm, 213 nm and 266 nm wavelengths. *Geostandards and Geoanalytical Research*, 29, 315–331. Available from: https://doi.org/10.1111/j.1751-908X.2005.tb00903.x

Hamann, Y., Wulf, S., Ersoy, O., Ehrmann, W., Aydar, E. & Schmiedl, G. (2010) First evidence of a distal early Holocene ash layer in Eastern Mediterranean deep-sea sediments derived from the Anatolian volcanic province. *Quaternary Research*, 73, 497–506. Available from: https://doi.org/10.1016/j.yqres.2009.12.004

Innocenti, Mazzuoli, F., Pasquare, R. et al. (1975) The Neogene calc-alcaline volcanism of Central Anatolia: geochronological data on Kayseri–Nigde area. *Geological Magazine*, 112, 349–360. Available from: https://doi.org/10.1017/S0016756800046744

Jarosewich, E. (2002) Smithsonian microbeam standards. *Journal of Research of the National Institute of Standards and Technology*, 107, 681–685. Available from: https://doi.org/10.6028/jres.107.054

Jochum, Weis, K.P., Stoll, U. et al. (2011) Determination of reference values for NIST SRM 610–617 glasses following ISO guidelines. *Geostandards and Geoanalytical Research*, 35, 397–429. Available from: https://doi.org/10.1111/j.1751-908X.2011.00120.x

Kearney, R.J., Albert, P.G., Staff, R.A., Magyari, E.K., Pál, I., Veres, D. et al. (2024) At an important tephrostratigraphic crossroads: cryptotephra in Late Glacial to Early Holocene lake sediments from the Carpathian Mountains, Romania. *Quaternary Science Reviews*, 330. 108558. Available from: https://doi.org/10.1016/j.quascirev.2024.108558.

Le Pennec, J.-L., Bourdier, J.-L., Froger, J.-L., Temel, A., Camus, G. & Gourgaud, A. (1994) Neogene ignimbrites of the Nevsehir plateau (Central Turkey): stratigraphy, distribution and source constraints. *Journal of Volcanology and Geothermal Research*, 63, 59–87. Available from: https://doi.org/10.1016/0377-0273(94)90018-3

Lowe, D.J. (2011) Tephrochronology and its application: a review. *Quaternary Geochronology*, 6, 107–153. Available from: https://doi.org/10.1016/j.quageo.2010.08.003

Monaco, L., Palladino, D.M., Gaeta, M., Marra, F., Sottili, G., Leicher, N. et al. (2021) Mediterranean tephrostratigraphy and peri-Tyrrhenian explosive activity revaluated in light of the 430–365 ka record from Fucino Basin (central Italy). *Earth-Science Reviews*, 220, 103706. Available from: https://doi.org/10.1016/j.earscirev.2021.103706.

Neugebauer, I., Wulf, S., Schwab, M.J., Serb, J., Plessen, B., Appelt, O. et al. (2017) Implications of S1 tephra findings in Dead Sea and Tayma palaeolake sediments for marine reservoir age estimation and palaeoclimate synchronisation. *Quaternary Science Reviews*, 170, 269–275. Available from: https://doi.org/10.1016/j.quascirev.2017.06.020

Nowaczyk, N.R., Arz, H.W., Frank, U. et al. (2012) Dynamics of the Laschamp geomagnetic excursion from Black Sea sediments. *Earth and Planetary Science Letters* 351–352, 54–69. Available from: https://doi.org/10.1016/j.epsl.2012.06.050

Olmstead, A.T.E., Charles, B.B. & Wrench, J. (1907) Climbed a historic cone. *Cornell Daily Sun* (Vol. 27, No. 102, 16 February 1907). Available from: https://cdsun.library.cornell.edu/?a=d&d=CDS19070216.2.28.9

Orsi, G. (2022) Volcanic and deformation history of the Campi Flegrei volcanic field, Italy. In: Orsi, G., D'Antonio, M. & Civetta, L., eds *Campi Flegrei. Active Volcanoes of the World*. Berlin, Heidelberg: Springer. https://doi.org/10.1007/978-3-642-37060-1_1

Orsi, G., Di Vito, M.A. & Isaia, R. (2004) Volcanic hazard assessment at the restless Campi Flegrei caldera. *Bulletin of Volcanology*, 66, 514–530. Available from: https://doi.org/10.1007/s00445-003-0336-4

Pasquarè, G., Poli, S., Vezzoli, L. & Zanchi, A. (1988) Continental arc volcanism and tectonic setting in Central Anatolia, Turkey. *Tectonophysics*, 146, 217–230. Available from: https://doi.org/10.1016/0040-1951(88)90092-3

Paton, C., Woodhead, J.D., Hellstrom, J.C., Hergt, J.M., Greig, A. & Maas, R. (2010) Improved laser ablation U-Pb zircon geochronology through robust downhole fractionation correction. *Geochemistry, Geophysics, Geosystems*, 11, Q0AA06. Available from: https://doi.org/10.1029/2009GC002618

Pedrazzi, D., Sunye-Puchol, I., Aguirre-Díaz, G., Costa, A., Smith, V.C., Poret, M. et al. (2019) The Ilopango Tierra Blanca Joven (TBJ) eruption, El Salvador: volcano-stratigraphy and physical characterization of the major Holocene event of Central America. *Journal of Volcanology and Geothermal Research*, 377, 81–102. Available from: https://doi.org/10.1016/j.jvolgeores.2019.03.006

Petersen, G.M., Büyükakpinar, P., Vera Sanhueza, F.O., Metz, M., Cesca, S., Akbayram, K. et al. (2023) The 2023 Southeast Türkiye seismic sequence: Rupture of a complex fault network. *The Seismic Record*, 3(2), 134–143. Available from: https://doi.org/10.1785/0320230008

Pistolesi, M., Isaia, R., Marianelli, P., Bertagnini, A., Fourmentraux, C., Albert, P.G. et al. (2016) Simultaneous eruptions from multiple vents at Campi Flegrei (Italy) highlight new eruption processes at calderas. *Geology*, 44(6), 487–490. Available from: https://doi.org/10.1130/G37870.1

Raczek, I., Stoll, B., Hofmann, A.W. & Peter Jochum, K. (2001) High-Precision Trace Element Data for the USGS Reference Materials BCR-1, BCR-2, BHVO-1, BHVO-2, AGV-1, AGV-2, DTS-1, DTS-2, GSP-1 and GSP-2 by ID-TIMS and MIC-SSMS. *Geostandards Newsletter*, 25, 77–86. Available from: https://doi.org/10.1111/j.1751-908X.2001.tb00789.x

Reimer, P.J., Austin, W.E.N., Bard, E., Bayliss, A., Blackwell, P.G., Bronk Ramsey, C. et al. (2020) The IntCal20 Northern Hemisphere radiocarbon age calibration curve (0–55 cal kBP). *Radiocarbon*, 62(4), 725–757. Available from: https://doi.org/10.1017/RDC.2020.41

Rossignol-Strick, M., Nesteroff, W., Olive, P. & Vergnaud Grazzini, C. (1982) After the deluge: mediterranean stagnation and sapropel formation. *Nature*, 295, 105–110. Available from: https://doi.org/10.1038/295105a0

Sarıkaya, M.A., Çiner, A., Zreda, M., Şen, E. & Ersoy, O. (2019) Chlorine degassing constrained by cosmogenic ^{36}Cl and radiocarbon dating of early Holocene rhyodacitic lava domes on Erciyes stratovolcano, central Turkey. *Journal of Volcanology and Geothermal Research*, 369, 263–275. Available from: https://doi.org/10.1016/j.jvolgeores.2018.11.029

Satow, C., Tomlinson, E.L., Grant, K.M., Albert, P.G., Smith, V.C., Manning, C.J. et al. (2015) A new contribution to the Late Quaternary tephrostratigraphy of the Mediterranean: Aegean Sea core LC21. *Quaternary Science Reviews*, 117, 96–112. Available from: https://doi.org/10.1016/j.quascirev.2015.04.005

Scarpati, C., Perrotta, A., Lepore, S. & Calvert, A. (2013) Eruptive history of Neapolitan volcanoes: constraints from 40Ar–39Ar dating. *Geological Magazine*, 150(3), 412–425. Available from: https://doi.org/10.1017/S0016756812000854

Scarpati, C., Sparice, D. & Perrotta, A. (2020) Dynamics of large pyroclastic currents inferred by the internal architecture of the Campanian Ignimbrite. *Scientific Reports*, 10. 22230. Available from: https://doi.org/10.1038/s41598-020-79164-7.

Schmidt, A. (2007) Deep-sea ecosystem variability in the Eastern Levantine Basin during the Late Quaternary as revealed by benthic foraminifera and stable isotopes PhD Thesis, Universit ät Leipzig.

Şen, E., Kürkcüoğlu, B., Aydar, E., Gourgaud, A. & Vincent, P.M. (2003) Volcanological evolution of Mount Erciyes stratovolcano and origin of the Valibaba Tepe ignimbrite (Central Anatolia, Turkey). *Journal of Volcanology and Geothermal Research*, 125, 225–246. Available from: https://doi.org/10.1016/S0377-0273(03)00110-0

Seropian, G., Schipper, C.I., Harmon, L.J., Smithies, S.L., Kennedy, B.M., Castro, J.M. et al. (2021) A century of ongoing silicic volcanism at Cordón Caulle, Chile: new constraints on the magmatic system involved in the 1921–1922, 1960 and 2011–2012 eruptions. *Journal of Volcanology and Geothermal Research*, 420, 107406. Available from: https://doi.org/10.1016/j.jvolgeores.2021.107406.

Smith, V.C., Costa, A., Aguirre-Díaz, G., Pedrazzi, D., Scifo, A., Plunkett, G. et al. (2020) The magnitude and impact of the 431 CE Tierra Blanca Joven eruption of Ilopango, El Salvador. *Proceedings of the National Academy of Sciences*, 117(42), 26061–26068. Available from: https://doi.org/10.1073/pnas.2003008117

Smith, V.C., Isaia, R. & Pearce, N.J.G. (2011) Tephrostratigraphy and glass compositions of post-15 kyr Campi Flegrei eruptions: implications for eruption history and chronostratigraphic markers. *Quaternary Science Reviews*, 30, 3638–3660. Available from: https://doi.org/10.1016/j.quascirev.2011.07.012

Suñe-Puchol, I., Aguirre-Díaz, G.J., Dávila-Harris, P., Miggins, D.P., Pedrazzi, D., Costa, A. et al. (2019a) The Ilopango caldera complex, El Salvador: origin and early ignimbrite-forming eruptions of a graben/pull-apart caldera structure. *Journal of Volcanology and Geothermal Research* 371, 1–19. Available from: https://doi.org/10.1016/j.jvolgeores.2018.12.004

Suñe-Puchol, I., Aguirre-Díaz, G.J., Pedrazzi, D., Dávila-Harris, P., Miggins, D.P., Costa, A. et al. (2019b) Stratigraphic revision of the complete eruptive sequence and recurrence of large explosive eruptions. The Ilopango Caldera Complex (El Salvador). *Journal of Volcanology and Geothermal Research* 374, 100–119. Available from: https://doi.org/10.1016/j.jvolgeores.2019.02.011

Sunyé-Puchol, I., Hodgetts, A.G.E., Watt, S.F.L., Arce, J.L., Barfod, D.N., Mark, D.F. et al. (2022) Reconstructing the middle to late Pleistocene explosive eruption histories of Popocatépetl, Iztaccíhuatl and Tláloc-Telapóon volcanoes in Central Mexico. *Journal of Volcanology and Geothermal Research* 421(1), 1–29. Available from: https://doi.org/10.1016/j.jvolgeores.2021.107413

Whitney, D.L., Delph, J.R., Thomson, S.N., Beck, S.L., Brocard, G.Y., Cosca, M.A. et al. (2023) Breaking plates: creation of the East Anatolian fault, the Anatolian plate, and a tectonic escape system. *Geology*, 51, 673–677. Available from: https://doi.org/10.1130/G51211.1

Woodhead, J.D., Hellstrom, J., Hergt, J.M., Greig, A. & Maas, R. (2007) Isotopic and elemental imaging of geological materials by laser ablation Inductively coupled Plasma mass spectrometry. *Geostandards and Geoanalytical Research*, 31, 331–343. Available from: https://doi.org/10.1111/j.1751-908X.2007.00104.x

Wulf, S., Keller, J., Satow, C., Gertisser, R., Kraml, M., Grant, K.M. et al. (2020) Advancing Santorini's tephrostratigraphy: new glass geochemical data and improved marine-terrestrial tephra correlations for the past ~360 kyrs. *Earth-Science Reviews*, 200, 102964. Available from: https://doi.org/10.1016/j.earscirev.2019.102964